



# Synthesis and characterization of carbon black/manganese oxide air cathodes for zinc-air batteries



Po-Chieh Li <sup>a</sup>, Chi-Chang Hu <sup>a,\*</sup>, Tai-Chou Lee <sup>b</sup>, Wen-Sheng Chang <sup>c</sup>, Tsin Hai Wang <sup>d</sup>

<sup>a</sup> Laboratory of Electrochemistry & Advanced Materials, Department of Chemical Engineering, National Tsing-Hua University, 101, Section 2, Kuang-Fu Road, Hsin-Chu 30013, Taiwan

<sup>b</sup> Department of Chemical and Materials Engineering, National Central University, Tao-Yuan, Taiwan

<sup>c</sup> Green Energy and Environment Research Laboratories, Industrial Technology Research Institute, Hsin-Chu, Taiwan

<sup>d</sup> Department of Biomedical Engineering and Environmental Sciences, National Tsing-Hua University, Hsin-Chu 300, Taiwan

## HIGHLIGHTS

- The average electron transfer number of the ORR on  $\alpha$ -MnO<sub>2</sub> is close to 4.
- Transformation from  $\alpha$ -MnO<sub>2</sub> to MnOOH is significant with XC72 content larger than 50 wt%.
- The composite with the XC72/ $\alpha$ -MnO<sub>2</sub> weight ratio equal to 1 shows the highest ORR activity.
- A discharge peak power density, 67.51 mW cm<sup>-2</sup>, is obtained for a Zn-air battery.
- A power density of 23.0 mW cm<sup>-2</sup> and specific capacity of 798  $\pm$  20 mAh g<sup>-1</sup> are obtained at 20 mA cm<sup>-2</sup>.

## ARTICLE INFO

### Article history:

Received 3 April 2014

Received in revised form

18 June 2014

Accepted 19 June 2014

Available online 7 July 2014

### Keywords:

Zinc-air battery

Manganese dioxide

Alpha phase

Oxygen reduction reaction

Carbon black

## ABSTRACT

Due to the poor electric conductivity but the excellent catalytic ability for the oxygen reduction reaction (ORR), manganese dioxide in the  $\alpha$  phase (denoted as  $\alpha$ -MnO<sub>2</sub>) anchored onto carbon black powders (XC72) has been synthesized by the reflux method. The specific surface area and electric conductivity of the composites are generally enhanced by increasing the XC72 content while the high XC72 content will induce the formation of MnOOH which shows a worse ORR catalytic ability than  $\alpha$ -MnO<sub>2</sub>. The ORR activity of such air cathodes have been optimized at the XC72/ $\alpha$ -MnO<sub>2</sub> ratio equal to 1 determined by the thermogravimetric analysis. By using this optimized cathode under the air atmosphere, the quasi-steady-state full-cell discharge voltages are equal to 1.353 and 1.178 V at 2 and 20 mA cm<sup>-2</sup>, respectively. Due to the usage of ambient air rather than pure oxygen, this Zn-air battery shows a modestly high discharge peak power density (67.51 mW cm<sup>-2</sup>) meanwhile the power density is equal to 47.22 mW cm<sup>-2</sup> and the specific capacity is more than 750 mAh g<sup>-1</sup> when this cell is operated at 1 V.

© 2014 Elsevier B.V. All rights reserved.

## 1. Introduction

Metal-air batteries [1–5] have attracted great attention in recent years because they have been demonstrated to meet the required energy density (>400 mAh g<sup>-1</sup>) of electric vehicles (EVs). Metal-air batteries generally show the great advantages of high theoretical energy density (e.g., 1312 Wh kg<sup>-1</sup> for Zn-air batteries, excluding oxygen) and specific capacity (820 mAh g<sup>-1</sup>) [3] because they are considered to be a hybrid cell of batteries and fuel cells. Similar to fuel cells, the air cathode employs a gas diffusion layer to obtain the

unlimited and free supply of oxygen from ambient air which is not stored in the device, resulting in the high energy density. On the other side, many kinds of metals, such as zinc [1,3–5], aluminum [5–8], lithium [2,4,5,9], and magnesium [5] have been widely employed as the anode of the metal-air batteries. Among these high energy-density power sources, Zn-air batteries are the most developed devices for both the small cells (e.g., for mobile phones and laptops) and the large module (for EVs). However, there are, at least, three challenges to be overcome or circumvented in order to meet the application demands of the modern society: (1) Zn dendrites during the charging process [10]; (2) the loss in the hydrophobic property of the air cathode due to accumulation of carbonate salts; and (3) the electrocatalytic and rechargeable properties of the air cathode [1,11].

\* Corresponding author. Tel./fax: +886 3 5736027.

E-mail address: [cchu@che.nthu.edu.tw](mailto:cchu@che.nthu.edu.tw) (C.-C. Hu).

URL: <http://mx.nthu.edu.tw/0732cchu/>

Since the air cathode is one of the key factors influencing the overall performances of Zn-air batteries [12], developing a suitable ORR catalyst on the cathode is very important in improving the performances of Zn-air batteries. Furthermore, the ORR on the cathode is a complicated reaction with slow kinetics at room temperature either in acidic or alkaline solutions. Until now, the best and most frequently used catalysts for the ORR are Pt-based materials [13], while its high price and scarcity make the Pt-based catalysts be practically inapplicable. Accordingly, it is desirable to use cost-effective catalysts, e.g. Co-based catalysts [14,15], Fe-based catalysts [16], Mn-based catalysts [17,18], and certain perovskite catalysts [1,19] to replace the expensive Pt-based catalysts.

Manganese dioxide [20–23] has been considered to be an attractive catalyst material for the cathode of metal-air batteries because of its low toxicity, low cost, environmental friendliness, and considerable activity toward the ORR. Manganese dioxide can be operated effectively in aqueous [21,24] and non-aqueous [25,26] systems, and generally exhibits a better efficiency in the alkaline electrolytes [3,27]. Meanwhile the ultimate performance and application of  $\text{MnO}_2$  have been found to be affected by its microstructures (e.g., particle shape, size, and crystalline phases, etc.). For instance, the catalytic performance of  $\text{MnO}_2$  has been reported to follow the sequences:  $\alpha > \beta > \gamma$  phases of  $\text{MnO}_2$  [28] or  $\alpha > \delta > \gamma > \lambda > \beta$  phases of  $\text{MnO}_2$  [29]. Fortunately, both reports were in agreement with that  $\alpha$ - $\text{MnO}_2$  possesses the highest catalytic activity for the ORR in the Zn-air batteries. According to the literature [20],  $\alpha$ - $\text{MnO}_2$  possesses a large tunnel structure ( $2 \times 2$ ) which makes ion transfer easily in the lattice framework, further promoting the ORR rate. Furthermore, there are more defects and hydroxyl groups on  $\alpha$ - $\text{MnO}_2$  surface, which are favorable for the adsorption/desorption of oxygen molecules and the dissociation of the oxygen double bond [28,30]. Although  $\alpha$ - $\text{MnO}_2$  shows a better ORR catalytic activity, its electric conductivity is very poor. In order to solve this issue, adding carbon black into  $\text{MnO}_2$  is usually employed to increase the electric conductivity and surface area of the resultant composites [21,24,31,32].

This work aims to use the reflux method with three precursors (i.e., potassium permanganate, manganese sulfate, and XC72 carbon black) to prepare  $\alpha$ - $\text{MnO}_2$ /XC72 composite samples. The electrocatalytic activity of  $\alpha$ - $\text{MnO}_2$ /XC72 composites was optimized by varying the amount of XC72 carbon black meanwhile the effect of the  $\alpha$ - $\text{MnO}_2$ /XC72 ratio on the average electron transfer of the ORR was systematically investigated. Finally, the full cell performances of a Zn-air battery with various  $\alpha$ - $\text{MnO}_2$ /XC72 electrocatalysts were characterized in this work.

## 2. Experimental details

### 2.1. Preparation of $\alpha$ - $\text{MnO}_2$ /XC72 electrocatalysts

XC72 carbon black (Vulcan XC-72, Cabot Corp., USA),  $\text{KMnO}_4$  (Showa Chemical Industry Co., Ltd.),  $\text{MnSO}_4 \cdot \text{H}_2\text{O}$  (Showa Chemical Industry Co., Ltd.), and Nafion<sup>®</sup> perfluorinated resin solution (5 wt% in a mixture of water and lower aliphatic alcohols with 45% water), ethylene glycol (Hayashi Pure Chemical Industry Co., Ltd.), KOH (Showa Chemical Industry Co., Ltd.) were all analytical grade and used without any further purification. Carbon paper (SGL carbon paper 10AA, 4 cm  $\times$  4 cm) was used as the substrate of the air cathode. A zinc foil (Alfa Aesar, 0.25 mm thick) was employed as the anode in the Zn-air battery.

Alpha- $\text{MnO}_2$ /XC72 electrocatalysts were prepared from a mixture consisting of XC72 powders (in various amounts: 0, 1, 2, 3, 4, 5, 6 g) and 4.056 g  $\text{MnSO}_4 \cdot \text{H}_2\text{O}$  powders into a three-necked round bottom flask. Then, 3.792 g  $\text{KMnO}_4$  powders were

dissolved and stirred in a 60-ml de-ionized (DI) water to form a 0.4 M  $\text{KMnO}_4$  solution. This  $\text{KMnO}_4$  solution was added slowly into the three-necked round flask containing the well-mixed XC72 and  $\text{MnSO}_4 \cdot \text{H}_2\text{O}$  powders. Finally, the above mixtures were stirred at 100 °C for 20 h. After the above steps, the solution was filtered and washed with DI water several times by a high-speed centrifuge (at 11,000 rpm, 10 min) to remove the excess  $\text{K}^+$ . The final products were obtained by drying in an oven at 85 °C overnight. The  $\alpha$ - $\text{MnO}_2$ /XC72 electrocatalysts prepared from the solutions containing 0, 1, 2, 3, 4, 5, 6 g of XC72 were labeled as a0, a1, a2, a3, a4, a5, and a6, respectively.

### 2.2. Materials characterization

The morphologies and microstructures of  $\alpha$ - $\text{MnO}_2$  and composites were examined using a field-emission scanning electron microscope (FE-SEM, Hitachi S-4200) and a transmission electron microscope (TEM, JEOL JEM-2010). The powder X-ray diffraction patterns were measured from an X-ray diffractometer (Cu  $K_\alpha$ , Ultima IV, Rigaku) at an angular speed of  $(2\theta) 1^\circ \text{min}^{-1}$ . The Brunauer-Emmett-Teller (BET) method was utilized to calculate the specific surface areas ( $S_{\text{BET}}$ ) using the adsorption data from the  $\text{N}_2$  adsorption/desorption isotherms in a relative pressure range from 0.02 to 0.2 (Quantachrome Instruments NOVA 1200e). Prior to running  $\text{N}_2$  adsorption/desorption isotherms, all samples have been degassed at 85 °C for 6 h. By the Barrett-Joyner-Halenda (BJH) model, the pore volumes and pore size distributions in the mesopore range ( $>2$  nm) were derived from the adsorption branches of the isotherms, and the total pore volumes ( $V_t$ ) were estimated from the adsorbed amount at a relative pressure,  $P/P_0$ , equal to 0.995. The carbon content of composites was determined by thermogravimetric analysis (TGA, TA Instruments SDT Q600), which was performed in an air flow at  $10^\circ \text{C min}^{-1}$  from room temperature to 800 °C. Note that all sample powders employed for the TGA analysis did not contain any ethylene glycol because this compound was only added in the step of air cathode preparation.

### 2.3. Preparation of $\alpha$ - $\text{MnO}_2$ /XC72 air cathodes

An air cathode includes a catalyst layer (on the electrolyte side) and a gas-diffusion layer (on the air side; i.e., the 10AA carbon paper). The paste of the electrocatalyst powders was a homogeneous mixture containing 0.1 g  $\alpha$ - $\text{MnO}_2$ /XC72 powders, 0.035 g Nafion, and 0.25 g ethylene glycol. This paste was coated onto the 4 cm  $\times$  4 cm 10AA carbon paper to form an air cathode sheet with an exposed surface area of 2 cm  $\times$  2 cm for the electrocatalysts by means of the doctor-blade method. Finally, the air electrodes were dried in an oven at 85 °C for 24 h.

### 2.4. Electrochemical measurements

Electrochemical analyses (e.g., polarization curves and rotating ring-disk electrode (RRDE) voltammetry) were measured by electrochemical system modules (CH Instruments 660C or CH Instruments 730D) at a scan rate of  $5 \text{ mV s}^{-1}$ . The exposed area of all air cathodes to the 0.1 M KOH electrolyte was 4 cm<sup>2</sup> for polarization and 0.247 cm<sup>2</sup> for the RRDE. An Ag/AgCl electrode (Argenthal, 3 M KCl, 0.207 V vs. SHE at 25 °C) in a Luggin capillary was used as the reference and a large piece of platinum gauze was employed as the counter electrode. The Luggin capillary was used to minimize errors due to  $iR$  drop in the electrolytes. For the RRDE voltammetric measurements, the RRDE was polished with  $\text{Al}_2\text{O}_3$  slurry and cleaned in ultrasonic bath with ethanol and de-ionized water before coating the electrocatalyst. Suspensions of  $\alpha$ - $\text{MnO}_2$  or  $\alpha$ - $\text{MnO}_2$ /XC72 powders were prepared by adding 1.32 mg of sample

powders, 8 ml of 5 wt% Nafion® (E.I. du Pont de Nemours & Co., USA) and 0.392 ml of 99.5% ethanol (Kanto Chemical Co. Inc., Japan). The resultant solution was agitated in an ultrasonic bath till the solution dispersed uniformly. The homogeneous suspensions were coated on the glassy-carbon (GC) disk electrode for the RRDE voltammetry with the loading mass of  $0.2 \text{ mg cm}^{-2}$ . The 0.1 M KOH electrolyte was bubbled with  $\text{O}_2$  or  $\text{N}_2$  gas (purity 99.995%) for more than 30 min before each RRDE test. During the RRDE measurement, the solution was under the  $\text{O}_2$  or  $\text{N}_2$  atmosphere at room temperature. The potential of linear sweep voltammetry (LSV) applied to the disk electrode was varied from 1.17 to 0.18 V vs. RHE at  $5 \text{ mV s}^{-1}$  meanwhile the potential on the ring electrode was fixed at 1.05 V vs. RHE in order to efficiently capture the intermediates of oxygen reduction on the disk electrode.

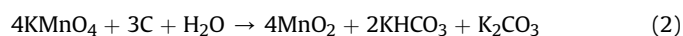
The LSV polarization curves of air cathodes and the Zn-air battery discharge curves were respectively measured in 0.1 M and 6 M KOH, where a Zn foil and the  $\alpha\text{-MnO}_2/\text{XC72}$  air electrode served as the anode and cathode, respectively. The gas-diffusion layer of the air cathodes was directly exposed to the ambient air in the above LSV and full-cell discharge tests. The batteries were galvanostatically discharged at three current densities (2, 10, and  $20 \text{ mA cm}^{-2}$ ) with respect to the electroactive area of the air cathode ( $2 \text{ cm} \times 2 \text{ cm}$ ) at room temperature. The specific discharge capacities of the cells were calculated on the basis of the consumed mass of the Zn foil. To avoid any unperceived disturbances, fresh air cathodes, Zn foils, and electrolytes were used in every measurement. All solutions used in this work were prepared with 18 M $\Omega$ -cm DI water produced by a reagent water system (Milli-Q SP, Japan).

### 3. Results and discussion

#### 3.1. Characterization of $\alpha\text{-MnO}_2/\text{XC72}$ electrocatalysts

To find the optimal mass ratio of the  $\alpha\text{-MnO}_2/\text{XC72}$  composite with the highest ORR activity, five kinds of Mn oxide/XC72 powders with different amounts of XC72 were successfully synthesized by the reflux method. Fig. 1 shows the typical XRD patterns of XC72 carbon black,  $\alpha\text{-MnO}_2$ , and Mn oxide/XC72. From pattern 1, there are two very broad peaks centered at  $24.9^\circ$  and  $43.6^\circ$ , corresponding to the poor graphite structure of XC72. The five characteristic peaks at  $28.84^\circ$ ,  $37.52^\circ$ ,  $41.96^\circ$ ,  $49.86^\circ$ , and  $60.27^\circ$  on pattern

2 reveal the formation of  $\alpha\text{-MnO}_2$  (JCPDS 44–0141). The XRD patterns of a1–a3 are very similar to pattern 2, revealing the formation of  $\alpha\text{-MnO}_2/\text{XC72}$  composites although the presence of a minor peak centered at ca.  $24.9^\circ$  implies the presence of certain MnOOH. Interestingly, when the carbon black content in the precursor solution is higher than 3 g (i.e., samples a4–a6), the diffraction intensities of MnOOH (JCPDS 41–1379) characteristic peaks at  $26.1^\circ$ ,  $33.9^\circ$ ,  $37.2^\circ$ ,  $51.2^\circ$ ,  $54.8^\circ$ ,  $54.9^\circ$ , and  $61.8^\circ$  are enhanced, revealing that the dominant phase of Mn oxides is MnOOH since the diffraction peaks at  $28.84^\circ$  and  $37.52^\circ$  are indicative of the  $\alpha\text{-MnO}_2$  phase. Therefore, the dominant phase of Mn oxides formed in the composite is significantly affected by the amount of XC72, which is never reported before. Note that  $\alpha\text{-MnO}_2$  has a general formula “ $\text{M}'\text{Mn}_x\text{O}_y$ ” where the atom ratio of  $y/x$  is equal to 2 and  $\text{M}'$  represents alkali metal ions such as  $\text{Li}^+$ ,  $\text{Na}^+$ , or  $\text{K}^+$ . Since one of the precursors is  $\text{KMnO}_4$ , the resultant  $\alpha\text{-MnO}_2$  may be more precisely expressed as  $\text{KMn}_x\text{O}_y$  (e.g.,  $\text{KMn}_8\text{O}_{16}$ ) [35]. Accordingly, the formation of  $\text{KMn}_8\text{O}_{16}$  (representing  $\alpha\text{-MnO}_2$ ) (Eq. (1)),  $\text{MnO}_2$  (Eq. (2)), and  $\text{MnOOH}$  (Eq. (3)) can be simply expressed as follow: [32–34]



where Eq. (3) may be catalyzed by excess XC72 although carbon is one of the reactants in Eq. (2). Unfortunately, the exact reasons why the dominant phase of Mn oxides in the Mn oxide/XC72 composites is controlled by the amount of XC72 are unclear. Note that the mean oxidation state of Mn in  $\text{KMn}_8\text{O}_{16}$  is not equal to 4 and this compound is considered to be a nonstoichiometric compound consisting of  $\text{Mn}^{4+}$  and minor  $\text{Mn}^{3+}$ . In fact, the detailed mechanism for the  $\text{KMn}_8\text{O}_{16}$  formation is not very clear and Eq. (1) is usually the acceptable and general equation for synthesizing  $\alpha\text{-MnO}_2$  in the literature.

The content of XC72 in the composites was determined by the thermo-gravimetric analysis (TGA) under an air flow. Fig. 2 shows the typical TGA curves of all samples from room temperature to  $800^\circ\text{C}$ . From curve 1, the minor weight loss, about 3.2%, from room temperature to  $250^\circ\text{C}$  is reasonably attributed to the dehydration of physically adsorbed and chemically bound water molecules on  $\alpha\text{-MnO}_2$  [36]. The further weight loss of ca. 4.07% in the temperature

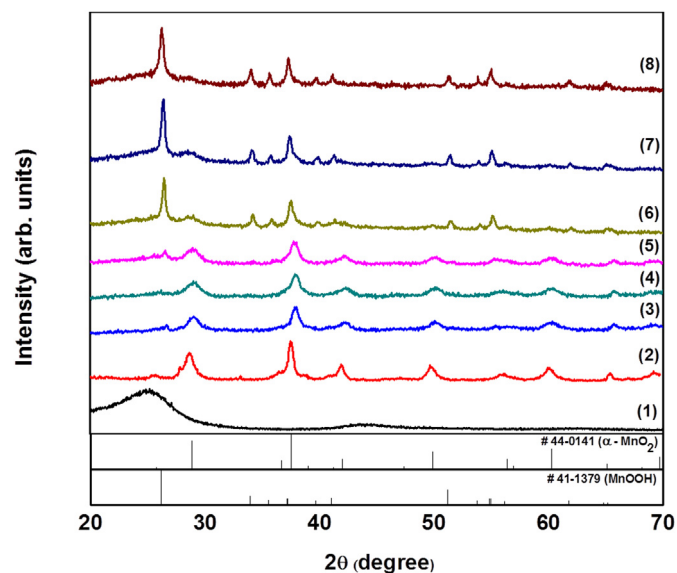


Fig. 1. The XRD patterns of (1) XC72, (2) a0, (3) a1, (4) a2, (5) a3, (6) a4, (7) a5, and (8) a6.

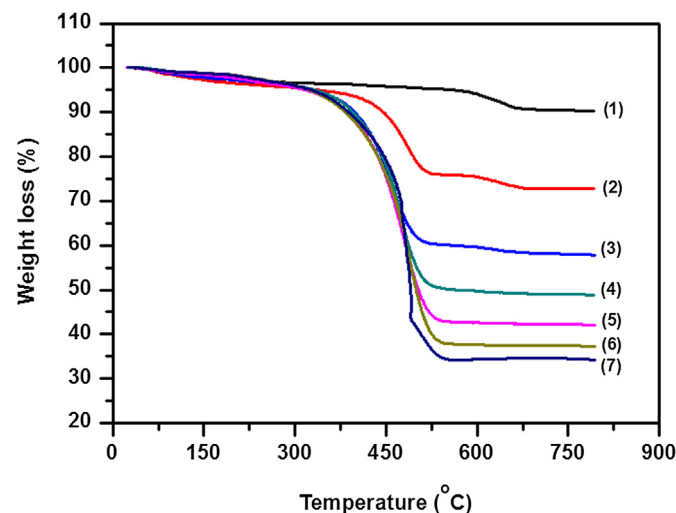


Fig. 2. The TGA curves of (1) a0, (2) a1, (3) a2, (4) a3, (5) a4, (6) a5, and (7) a6.

**Table 1**

The physicochemical properties of Mn oxide/XC72 composites.

	XC72	a0	a1	a2	a3	a4	a5	a6
XC72 (wt%)	100	0	21	38	50	56	61	64
$\alpha$ -MnO <sub>2</sub> (wt%)	0	100	79	62	50	44	39	36
BET surface area (m <sup>2</sup> g <sup>-1</sup> )	191	75	81	94	98	95	105	98
Mesopore volume (cc g <sup>-1</sup> )	0.292	0.271	0.344	0.445	0.338	0.393	0.337	0.317
Micropore volume (cc g <sup>-1</sup> )	0.133	0.057	0.064	0.072	0.072	0.071	0.078	0.073

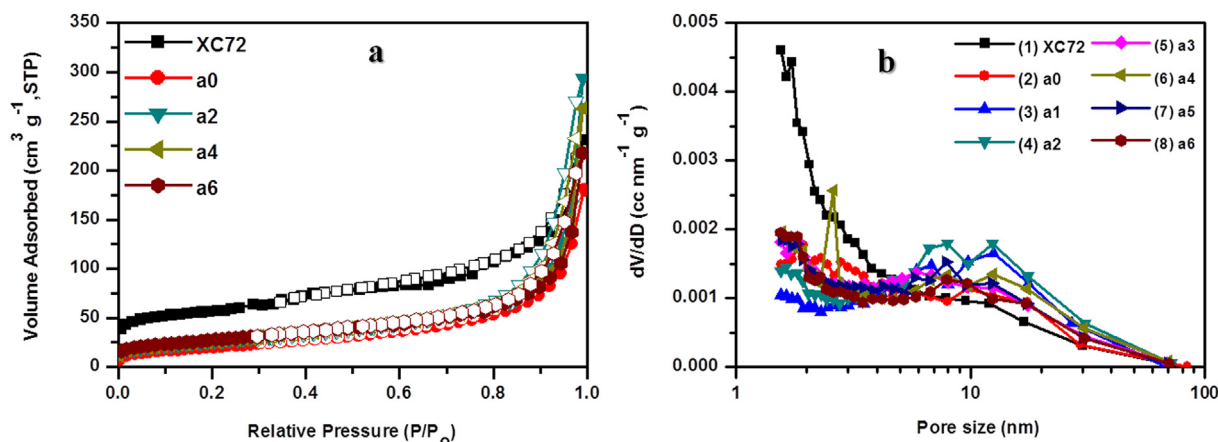
range from 575 to 675 °C corresponds to the removal of certain oxygen from  $\alpha$ -MnO<sub>2</sub> due to the phase transformation from  $\alpha$ -MnO<sub>2</sub> into Mn<sub>2</sub>O<sub>3</sub>. This phase transformation phenomenon is in good agreement with the reports in the literature [24,37]. From curves 2–6, XC72 could be completely decomposed at/before 550 °C. In addition, all sample powders employed for the TGA analysis did not contain any ethylene glycol. As a result, the concern that the residual ethylene glycol will react with  $\alpha$ -MnO<sub>2</sub> at elevated temperatures during the thermal analysis does not happen. Accordingly, the weight loss from 250 to 520 °C is attributable to the decomposition of XC72 into CO<sub>2</sub> and H<sub>2</sub>O. Based on this assumption, the amount of XC72 in samples a1–a6 varies from 21 to 65 wt% (see Table 1).

Fig. 3a shows the N<sub>2</sub> adsorption/desorption isotherms of four samples (XC72, a0, a2, a4 and a6) prepared in this work. The corresponding pore size distributions in the mesopore range shown in Fig. 3b were obtained from the Barrett-Joyner-Halenda (BJH) theory [38]. From Fig. 3a, the intercept of the N<sub>2</sub> adsorption/desorption isotherms (at P/P<sub>0</sub> close to 0) for XC72 is much larger than that of oxide and oxide/XC72 composites, suggesting that XC72 contains significant amount of micro-pores. In addition, the hysteresis loops on all isotherms are not very clear, indicating that the mesopores are relatively limited. Therefore, the pore volumes corresponding to mesopores on all samples are small although pure oxide and oxide/XC72 composites mainly contain the mesopores (see Fig. 3b and Table 1). The specific surface area are gradually increased with increasing the content of XC72 (Table 1), probably due to the fact that the specific surface area of XC72 (191 m<sup>2</sup> g<sup>-1</sup>) is much higher than that of Mn oxide (75 m<sup>2</sup> g<sup>-1</sup>). However, when the XC72 content is equal to/above 38 wt%, the specific surface area of composites becomes to be independent of the carbon black content. This phenomenon may be due to two effects. First, the variation in the XC72 content is not very large (only 16 wt% difference from a3 to a6). Hence, the effect of varying carbon black content becomes minor. Second, the pore size of XC72 is mainly distributed in the micropore range (<2 nm) and its micropore volume is 0.133 cc g<sup>-1</sup>.

However, the pore size distributions of a0–a6 are more uniform than that of XC72 and their micropore volumes are very small and similar. The above phenomena suggest the pore blocking of carbon black resulting from the accommodation of oxide particles on XC72.

The surface morphologies and microstructures of all samples prepared in this work have been systematically examined by means of FESEM and TEM analyses. For easy comparison purposes, the TEM images of samples a0, a1, a3, and a6 are shown in Fig. 4a–d, respectively. From Fig. 4a,  $\alpha$ -MnO<sub>2</sub> with minor amount of MnOOH prepared by the reflux method is of the nanowire form with its diameter and length around 15 and 300 nm, respectively. This interesting nanowire-like microstructure is commonly found for MnOOH [39,40] but unusual for  $\alpha$ -MnO<sub>2</sub>. From a comparison of Fig. 4a and b, the morphology of  $\alpha$ -MnO<sub>2</sub> is not significantly changed by introducing XC72 in the composite. This statement is supported by the similar morphology of sample a3 although the nanowire content is lower than that of sample a1. Due to the common nanowire morphology of MnOOH, sample a6 also shows a composite consisting of MnOOH nanowires and XC72 nanoparticles. However, the fast fourier transform (FFT) patterns (see insets of Fig. 4c and d) reveal that the dominant phases of oxides in samples a3 and a6 are  $\alpha$ -MnO<sub>2</sub> and MnOOH, respectively, which is consistent with the XRD results. From Fig. 4c and d, the measured d spacing of 0.682 and 0.232 nm are respectively assigned to the lattice spacing of the (110) plane of  $\alpha$ -MnO<sub>2</sub> and the (120) plane of MnOOH. Again, the dominant phase of Mn oxides formed in the Mn oxide/XC72 composites can be controlled by varying the amount of XC72 in the precursor solution.

Fig. 5a and b shows the morphologies of sample a3 before and after coating on the 10AA carbon paper, revealing no obvious changes by the coating procedure. In addition, certain  $\alpha$ -MnO<sub>2</sub> nanowires are visible in both SEM images. Based on the cross-section SEM image in Fig. 5c, the thickness of this  $\alpha$ -MnO<sub>2</sub>/XC72 coating on the 10AA carbon paper is approximately 170  $\mu$ m. Again, the unusual but interesting nanowire-like microstructure of  $\alpha$ -MnO<sub>2</sub> was successfully formed in sample a3.



**Fig. 3.** (a) Nitrogen adsorption/desorption isotherms and (b) pore size distributions of (1) a0, (2) a1, (3) a2, (4) a3, (5) a4, (6) a5, and (7) a6.

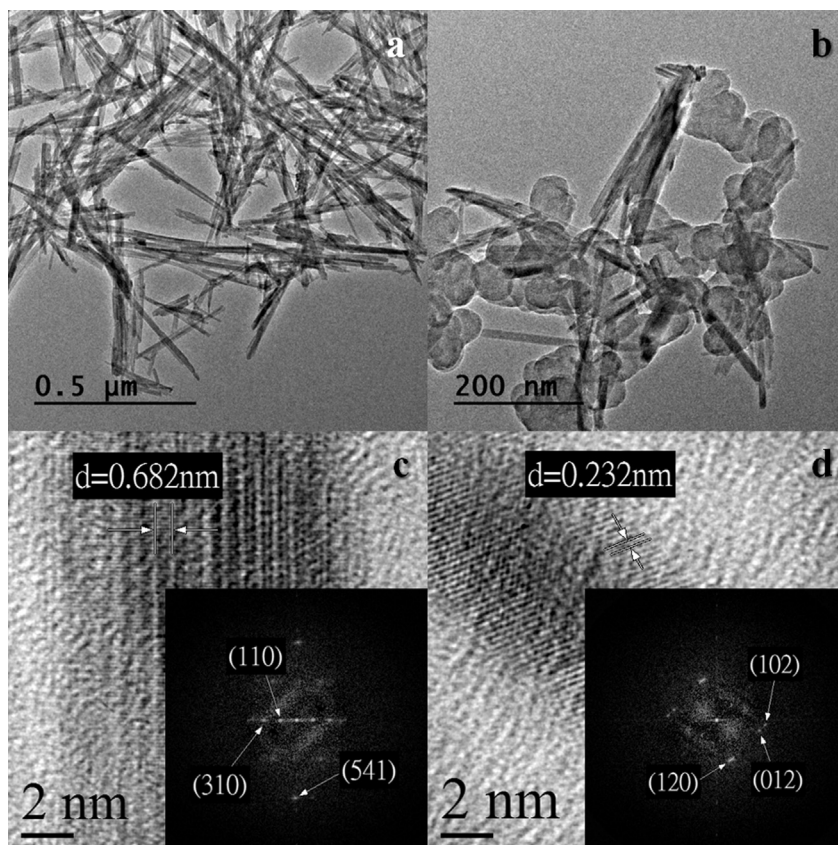


Fig. 4. The TEM images of (a) a0, (b) a1, and HRTEM images of (c) a3, and (d) a6 (inset are SAED patterns).

### 3.2. Characterization of the oxygen reduction reaction

The electrochemical kinetics of the ORR on all samples prepared in this work was examined by the RRDE voltammetry. In general, there are two typical pathways for the ORR mechanism: the direct four-electron pathway and the successive two-electron pathway [41]. The direct four-electron transfer pathway can be simply express as follow:



The successive two-electron pathway generally involves the formation of peroxide (e.g.,  $\text{HO}_2^-$ , see Eq. (5)) with the subsequent reduction of peroxide to  $\text{OH}^-$  (Eq. (6)) or the disproportionation of peroxide (Eq. (7)):



In alkaline electrolytes, classical noble metal catalysts (e.g., Pt or Pt alloys [13], Ag [42], and Au [43]) favor the four-electron transfer pathway. While most carbon materials as well as metal oxides and some transition metals favor the two-electron pathway [44–47] although certain N-doped carbons have been reported to run the four-electron transfer mechanism [46–51].

Fig. 6a and b respectively show the ring and disk currents against the applied electrode potential on the disk electrode (i.e., Fig. 6b shows the LSV curves of the disk electrode) on the RRDE. Here, the ring and disk currents respectively indicate the difference in the ring capture currents and disk voltammetric currents obtained from the solutions purged with  $\text{O}_2$  and  $\text{N}_2$  for longer than

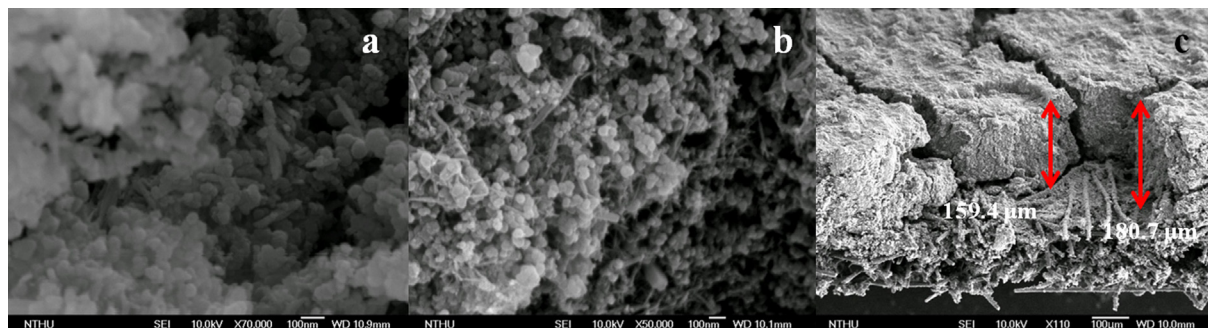
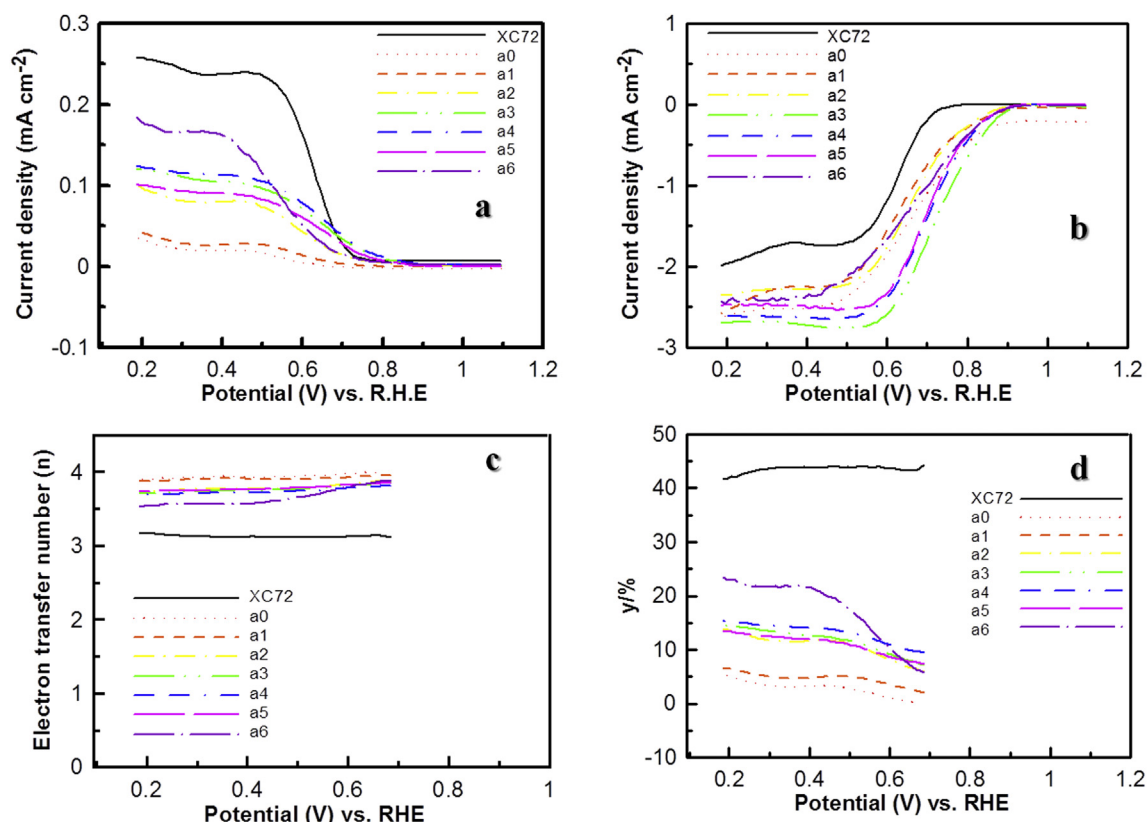


Fig. 5. The FESEM images of a3 (a) before and (b) after being coated onto the 10AA carbon paper, and (c) the cross-section image of an air cathode containing sample a3.



**Fig. 6.** (a) The ring currents against the electrode potential of the disk electrode and (b) the corresponding LSV curves of the disk electrode on the RRDE; (c) the mean electron transfer number ( $n$ ) of the ORR and (d) the peroxide yield percentage ( $\chi\%$ ) against the disk electrode potential of (1) a0, (2) a1, (3) a2, (4) a3, (5) a4, (6) a5, and (7) a6 in 0.1 M KOH.

30 min because the ring and disk currents obtained in the N<sub>2</sub>-purge electrolyte are considered to be the background responses. From an examination of both figures, three features need to be discussed here. First, the onset potential of the ORR on XC72 is significantly lower than that on both pure Mn oxide and Mn oxide/XC72 composites, revealing the electrocatalytic activity of  $\alpha$ -MnO<sub>2</sub> and MnOOH. The onset potential of the ORR for all electrocatalysts can be confirmed from the current responses on the ring electrode in Fig. 6a. Second, the order of samples with respect to decreasing the half-wave potential of the ORR (vs. RHE) is: a3 (0.72 V) > a4 ~ a5 (0.70 V) > a0 ~ a6 (0.67 V) > a2 (0.66 V) > a1 (0.65 V) > XC72 (0.63 V). This result indicates that the ORR activity of composites is simultaneously affected by the content of carbon black and the crystalline phase of oxides, probably due to the fact that the ORR activity is a function of the electrocatalytic (intrinsic) activity [52,53] and the specific surface area of composites [31]. Third, the limiting current density on the disk electrode is not directly proportional to the specific surface area of electrocatalysts because the order of samples with respect to decreasing the limiting current density of the ORR is: a3 (−2.73 mA cm<sup>-2</sup>) > a4 (−2.63 mA cm<sup>-2</sup>) > a0 (−2.52 mA cm<sup>-2</sup>) ≈ a5 (−2.52 mA cm<sup>-2</sup>) > a6 (−2.34 mA cm<sup>-2</sup>) > a2 (−2.28 mA cm<sup>-2</sup>) ~ a1 (−2.25 mA cm<sup>-2</sup>) > XC72 (−1.73 mA cm<sup>-2</sup> at 0.4 V). This is probably due to the significant influence of the mean electron transfer ( $n$ ) of the ORR. Based on the above results and discussion, sample a3 exhibits the highest ORR activity and is considered to be the optimal electrocatalyst for the Zn-air battery application. This optimized performance may be due to a combined effect of the specific surface area of composites (from a0 to a2) and the intrinsic catalytic activity of the dominant phase of Mn oxides in the composites (from a2 to a6).

The mean electron transfer number ( $n$ ) of the ORR and the peroxide yield ( $\chi$ , percentage of H<sub>2</sub>O<sub>2</sub> relative to the total product) are derived from the ring and disk current ( $I_R$  &  $I_D$ ) according to the following equations [22,54]:

$$n = \frac{4I_D}{I_D + (I_R/N)} \quad (8)$$

$$\chi(\text{H}_2\text{O}_2) \text{ in } \% = \frac{200 \times (I_R/N)}{I_D + (I_R/N)} \quad (9)$$

where  $I_D$ ,  $I_R$ , and  $N$  represent the disk current, ring current, and the current collection efficiency of the electrode ( $0.38 \pm 0.02$ ), respectively. The values of  $n$  and  $\chi$  for all of the samples are respectively shown in Fig. 6c and d as a function of the disk electrode potential (vs. RHE). Note that the mean electron transfer number of pure Mn oxide is above 3.9 in the potential range from ca. 0.7 to 0.2 V (vs. RHE, see Fig. 6c). The ORR on MnO<sub>2</sub> is believed to undergo the two-electron pathway but it has been called as a quasi-4e reduction pathway [22]. This statement is supported by the fact that MnO<sub>2</sub> has been reported to exhibit excellent ability for the disproportionation of HO<sub>2</sub><sup>-</sup> into OH<sup>-</sup> and O<sub>2</sub> via Eqs. (5) and (7) [17,18,29,45,52,55]. Hence, the mean electron transfer number of the ORR on nearly pure  $\alpha$ -MnO<sub>2</sub> approaches four. From Fig. 6c,  $n$  monotonously decreases with increasing the amount of XC72 (varying from ca. 3.9 to 3.15 for samples a0 to a6), which is due to the lower electrocatalytic activity of XC72 on the ORR in comparison with Mn oxides. Due to the quasi-4-electron transfer mechanism, the yield percentage of HO<sub>2</sub><sup>-</sup> ( $\chi\%$ ) on nearly pure  $\alpha$ -MnO<sub>2</sub> is the lowest (<5%) in the potential region from 0.7 to 0.2 V (see

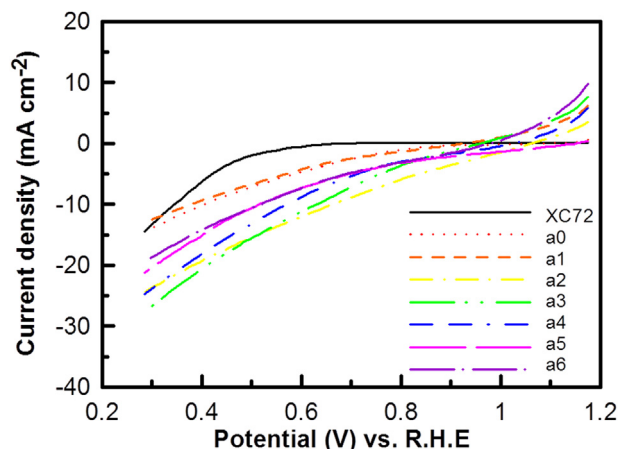


Fig. 7. The LSV curves measured at  $5 \text{ mV s}^{-1}$  in  $0.1 \text{ M KOH}$  for the air cathode containing (1) a0, (2) a1, (3) a2, (4) a3, (5) a4, (6) a5, and (7) a6. The gas diffusion layer side is directly exposed to the ambient air.

Fig. 6d). On the contrary, XC72 is a poor catalyst for decomposing  $\text{HO}_2^-$ , so its  $\chi\%$  is the highest value ( $>45\%$ ) in the applied potential range from ca. 0.7 to 0.2 V. Note curves 8 in Fig. 6c and d that the  $n$  and  $\chi$  values respectively decrease with the negative shift in the electrode potential of the disk electrode, which are not visible for the other samples. This phenomenon suggests that the amount of  $\text{MnOOH}$  is too low to effectively boost the disproportionation of  $\text{HO}_2^-$  into  $\text{OH}^-$  and  $\text{O}_2$  although the catalytic ability of  $\text{MnOOH}$  for the ORR is worse than that of  $\text{MnO}_2$  [52].

To confirm the electrochemical activity of all electrocatalysts for the ORR, the polarization curves of resultant air cathodes with their gas-diffusion layers directly exposed to the ambient air were measured in  $0.1 \text{ M KOH}$ . Typical LSV curves measured at  $5 \text{ mV s}^{-1}$  are shown in Fig. 7. In general, it is not easy to obtain the limiting current density from such polarization curves [56,57] although a relatively high current density (e.g.,  $-10 \text{ mA cm}^{-2}$ ) should result in the oxygen-diffusion issue. However, the order of air cathodes with respect to decreasing the current density of the ORR at 0.4 V is: a3 ( $-20.3 \text{ mA cm}^{-2}$ )  $>$  a2 ( $-19.0 \text{ mA cm}^{-2}$ )  $>$  a4 ( $-17.8 \text{ mA cm}^{-2}$ )  $>$  a5 ( $-14.8 \text{ mA cm}^{-2}$ )  $\sim$  a6 ( $-14.0 \text{ mA cm}^{-2}$ )  $>$  a0 ( $-10.0 \text{ mA cm}^{-2}$ )  $\sim$  a1 ( $-9.2 \text{ mA cm}^{-2}$ )  $>$  XC72 ( $-6.0 \text{ mA cm}^{-2}$ ), which is somewhat different from that with respect to decreasing the limiting current density from the RRDE voltammetry. In addition, the air cathode containing a2 exhibits the highest current density in the potential range from 1.0 to 0.5 V (vs. RHE) among all air cathodes. The above results may result from a combined effect of the three-phase

reaction zone and the electrocatalytic activity of composites although the exact reasons responsible for the above results are still unclear.

### 3.3. The discharge performance of Zn-air batteries

The typical discharge curve of a Zn-air battery using the air cathode consisting of a3 in  $6 \text{ M KOH}$  at  $10 \text{ mA cm}^{-2}$  is shown in Fig. 8a. In addition, the corresponding discharge curves of the Zn anode and air cathode are shown in the same figure to examine their individual performance. From the full-cell discharge curve, the cell voltage rapidly reaches the steady-state value (ca. 1.25 V), indicating the easy construction of the three-phase zone on the air cathode. This statement is supported by the fast approach of the steady discharge responses on the air cathode within 600 s on curve 2 in Fig. 8a since the potential of the Zn anode is approximately constant during the whole discharge period (curve 3). Therefore, the Mn oxide/XC72 air cathode is considered to be an excellent electrode for the ORR in both Zn-air batteries and alkaline fuel cells.

Fig. 8b and c shows the quasi-steady cell voltage as well as the corresponding discharge potentials of various air cathodes and a Zn anode in  $6 \text{ M KOH}$  at three current densities (i.e., 2, 10, and  $20 \text{ mA cm}^{-2}$ ), respectively. The discharge duration of all Zn-air batteries was fixed to be 600 s, meanwhile the discharge data shown here were obtained at the 600th second. From Fig. 8b, the quasi-steady cell voltage of Zn-air batteries is almost independent of the XC72 content when the current density is  $2 \text{ mA cm}^{-2}$ , indicating the minor polarization on all air cathodes. However, the influence of electrocatalysts becomes more obvious with increasing the current density from 2 to  $20 \text{ mA cm}^{-2}$ . This phenomenon is probably due to the transition from the activation polarization to the ohmic polarization (from 2 to  $10 \text{ mA cm}^{-2}$ ) and the severe ohmic polarization at  $20 \text{ mA cm}^{-2}$ . From a comparison of Fig. 8b and c, three interesting features have to be mentioned. First, the cell voltage of a Zn-air battery is mainly determined by the polarization behavior of the air cathode since the discharge potential of the Zn anode is very stable under any specified current density (see Fig. 8c). In other words, the discharge cell voltage of a Zn-air battery is mainly determined by the electrocatalytic performance of the air cathode which is a strong function of the composition and micro-structure of the ORR catalyst. Second, the cell with the air cathode containing sample a3 generates the highest cell voltages among all batteries under any specified current density. This result indicates the optimal XC72/ $\alpha$ - $\text{MnO}_2$  weight ratio in sample a3, which is consistent with the electrochemical performances from the RRDE results. However, it seems inconsistent with the polarization data

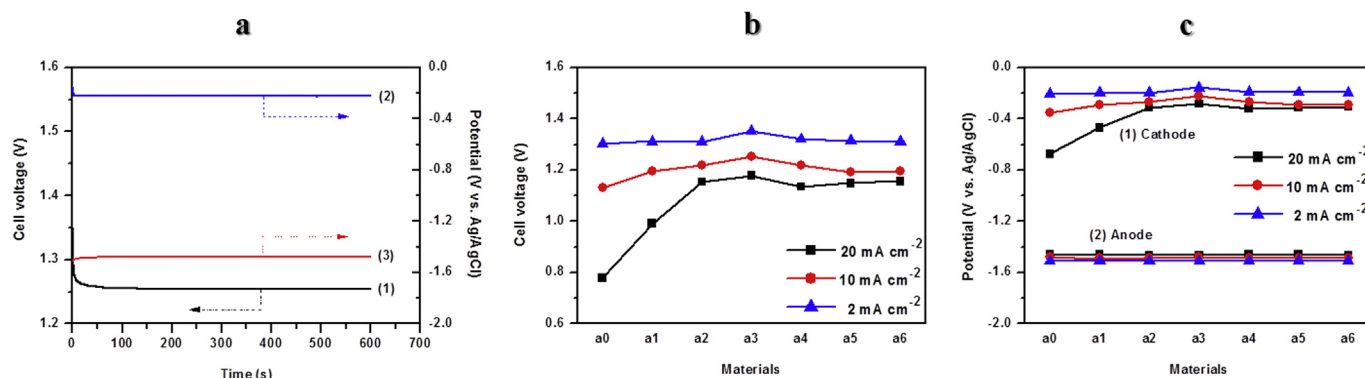


Fig. 8. (a) The discharge curves of (1) full cell, (2) air cathode, and (3) Zn anode for a Zn-air battery with an air cathode containing sample a3 in  $6 \text{ M KOH}$  at  $10 \text{ mA cm}^{-2}$ . The quasi-steady (b) cell voltage and (c) electrode potentials of (1) air cathode and (2) Zn anode measured from Zn-air batteries with the air cathode containing various ORR catalysts.

in Fig. 7 because the air cathode containing a2 exhibits the highest electrode potential at the current density lower than  $16 \text{ mA cm}^{-2}$  among all air cathodes. The above conflict phenomenon may be due to the measuring difference between the quasi-steady and potentiodynamic methods since the electrode potential of a2 from the polarization curve at  $10 \text{ mA cm}^{-2}$  is only slightly higher than that of a3. Third, the electrode potentials of the air cathodes containing samples a2–a6 are less sensitive to the discharge current density, especially in the high current density region, in comparison with a0 and a1. This effect results in the approximately constant cell voltage discharged at  $20 \text{ mA cm}^{-2}$  for the Zn-air batteries with the air cathodes containing samples a2–a6 (i.e., cell voltages between 1.13 and 1.17 V). Since the specific surface areas of samples a2–a6 are very similar (i.e., varying from  $94$  to  $105 \text{ m}^2 \text{ g}^{-1}$ ) and significantly higher than those of samples a0 ( $75 \text{ m}^2 \text{ g}^{-1}$ ) and a1 ( $81 \text{ m}^2 \text{ g}^{-1}$ ), the polarization behavior of the air cathode in the high current density region should be mainly determined by the specific surface area of electrocatalysts. However, because the yield percentage of  $\text{H}_2\text{O}_2$  for sample a6 is too high under the serve polarization condition (above 20%), the Zn-air battery may be seriously damaged by the free radicals coming from the decomposition of  $\text{H}_2\text{O}_2$ , which should be avoided.

From the above results and discussion, sample a3 has been concluded to be the optimal electrocatalyst with the highest activity for the ORR. Accordingly, a3 was chosen to be the model electrocatalyst for measuring the long-time discharge response of a Zn-air battery (see Fig. 9). Curves 1–3 in Fig. 9a respectively show the Zn-air battery discharged at 2, 10, and  $20 \text{ mA cm}^{-2}$ , meanwhile curves 2 and 3 show the continuous discharge curves of the batteries to the state where the Zn foil has been almost completely consumed. Clearly, the Zn-air battery with the cathode containing sample a3 can sustain more than 28 h without any obvious drop in the discharge plateau voltage, 1.3 V, at a constant current density of  $2 \text{ mA cm}^{-2}$ . Furthermore, the Zn-air battery can sustain about 11.5 and 6.5 h even at 10 and  $20 \text{ mA cm}^{-2}$  with the their discharge plateaus of 1.2 and 1.1 V, respectively. These results demonstrate the excellent discharge performance of the full cells, which is mainly contributed by the high ORR activity of the air cathode containing our excellent electrocatalyst. Note that the above difference in the total discharge capacity of two batteries is due to the mass difference between anodes although the exposed surface areas of both Zn foils are same. This reasonable phenomenon results from the fact that Zn is the limited reactant in the Zn-air batteries, which determines the total discharge capacity of full cells. This statement is strongly supported by the approximately

same specific capacity ( $798 \pm 20 \text{ mAh g}^{-1}$ ) of the above three Zn-air batteries from the results shown in Fig. 9a, where the specific capacity is normalized to the consumed mass of the Zn foil (see Fig. 9b). The above specific capacity data are very close to the theoretical specific capacity,  $820 \text{ mA g}^{-1}$ , revealing the excellent discharge performances, especially under the relatively high current densities of discharge.

Curves 1 and 2 in Fig. 10a respectively show the polarization curve and the plot of power density against the discharge current density for a Zn-air battery with an air cathode containing sample a3. From curve 1, the open circuit potential of this cell is about 1.44 V, which is about 0.2 V deviated from the theoretical value, reasonably attributed to the high activation overpotential of the ORR. The obvious drop in the cell voltage at current densities lower than ca.  $8 \text{ mA cm}^{-2}$  also indicates the activation polarization of this battery, mainly contributed from the air cathode. The linear decrease in the cell voltage with the current density at current densities larger than  $8 \text{ mA cm}^{-2}$  indicates the transition from the activation polarization situation to the ohmic polarization state. Moreover, the maximum power density ( $67.51 \text{ mW cm}^{-2}$ ) of this Zn-air battery occurring at a current density equal to  $105.25 \text{ mA cm}^{-2}$  is much higher than the values reported in the literature [58–62], indicating the successful development of an excellent air cathode although the modestly high power density of this cell employing the ambient air is much lower than the value of a cell supplied with pure oxygen [63]. To identify the stability of this Zn-air battery, another new cell was tested by a multi-current step method at five current densities: 0, 2, 10, 20, and  $40 \text{ mA cm}^{-2}$  (see Fig. 10b). The discharge curves of each step are smooth and stable in the whole discharge duration. The discharge cell voltages are equal to 1.44, 1.33, 1.23, 1.15, and 1.01 V at the current densities equal to 0, 2, 10, 20, and  $40 \text{ mA cm}^{-2}$ , respectively. The above results indicate that the Zn-air battery with the air cathode using sample a3 as the ORR catalyst can be operated stably in a wide range of current density; especially even at a current density of  $40 \text{ mA cm}^{-2}$ , the cell voltage of this battery is still above 1 V.

#### 4. Conclusions

The optimal Mn oxide/XC72 electrocatalyst contained about 50 wt% of XC72 meanwhile  $\alpha\text{-MnO}_2$  was the main crystalline phase in this optimized composite. When the amount of XC72 in the catalyst composites was equal to/above 56 wt%, the main phase of  $\alpha\text{-MnO}_2$  in the composites was transformed into MnOOH. In the RRDE electroanalyses, the mean electron transfer number of  $\alpha\text{-$

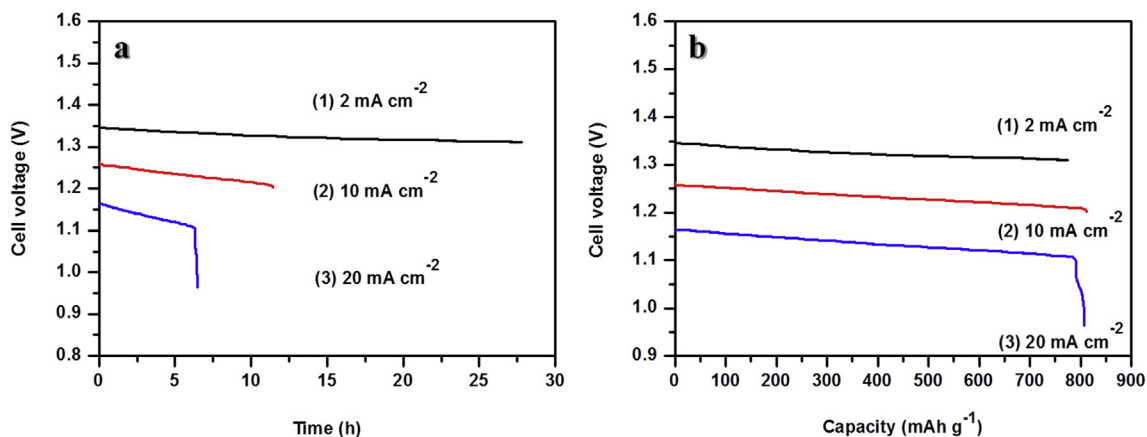
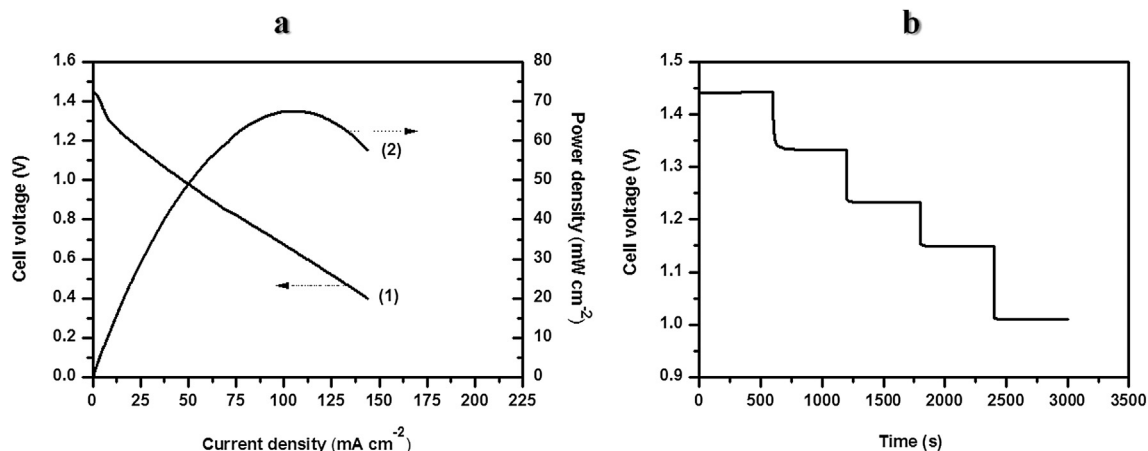


Fig. 9. The long-time discharge curves against (a) time and (b) specific capacity of Zn in 6 M KOH for a Zn-air battery with the air cathode containing sample a3, which was discharged at (1) 2, (2) 10, and (3)  $20 \text{ mA cm}^{-2}$ .



**Fig. 10.** (a) The polarization curve (1) and the plot of power density against the discharge current density (2) measured in 6 M KOH for a Zn-air battery with an air cathode containing sample a3. (b) The discharge curve of this cell at a current density of 0, 2, 10, 20, and 40  $\text{mA cm}^{-2}$  in 6 M KOH.

$\text{MnO}_2$  was about 3.95, revealing an excellent electrocatalyst toward the ORR. However, from the full cell discharge tests, electrochemical polarization of the air cathode in the high current density region was mainly determined by the specific surface area of electrocatalysts. The Zn-air battery with the air cathode containing the optimized electrocatalyst exhibited the specific capacity ( $798 \pm 20 \text{ mAh g}^{-1}$ ) close to the theoretical value ( $820 \text{ mAh g}^{-1}$ ) under various current densities. The maximum power density ( $67.51 \text{ mW cm}^{-2}$ ) of this Zn-air battery occurring at a current density equal to  $105.25 \text{ mA cm}^{-2}$  is much higher than the values of previous Zn-air batteries supplied with ambient air [58–62]. This Zn-air battery can be operated stably in a wide range of current density; especially 1 V was obtained at  $40 \text{ mA cm}^{-2}$ .

## Acknowledgments

This research was funded by the National Science Council, Taiwan under contract no. NSC 102-3113-P-194-003, 101-2221-E-007-112-MY3, 102-2221-E-007-120-MY3, the Ministry of Science and Technology, Taiwan under contract no. MOST 103-3113-E-194-002, and the boost program from the Low Carbon Energy Research Center of National Tsing Hua University, are gratefully acknowledged.

## References

- [1] V. Neburchilov, H. Wang, J.J. Martin, W. Qu, J. Power Sources 195 (2010) 1271–1291.
- [2] G. Girishkumar, B. McCloskey, A. Luntz, S. Swanson, W. Wilcke, J. Phys. Chem. Lett. 1 (2010) 2193–2203.
- [3] C. Chakkaravarthy, A. Waheed, H. Udupa, J. Power Sources 6 (1981) 203–228.
- [4] J.S. Lee, S. Tai Kim, R. Cao, N.S. Choi, M. Liu, K.T. Lee, J. Cho, Adv. Energy Mater. 1 (2011) 34–50.
- [5] M.A. Rahman, X. Wang, C. Wen, J. Electrochem. Soc. 160 (2013) A1759–A1771.
- [6] S. Yang, H. Knickle, J. Power Sources 112 (2002) 162–173.
- [7] Z. Solomon, N. Cochran, R.M. Mazgaj, J. Electrochem. Soc. 137 (1990) 1851–1857.
- [8] Y. Tang, L. Lu, H.W. Roesky, L. Wang, B. Huang, J. Power Sources 138 (2004) 313–318.
- [9] A. Kraysberg, Y. Ein-Eli, J. Power Sources 196 (2011) 886–893.
- [10] F.R. McLarnon, E.J. Cairns, J. Electrochem. Soc. 138 (1991) 645–656.
- [11] P. Sapkota, H. Kim, J. Indus. Eng. Chem. 15 (2009) 445–450.
- [12] S.S. Zhang, D. Foster, J. Read, J. Power Sources 195 (2010) 1235–1240.
- [13] H.A. Gasteiger, S.S. Kocha, B. Sompalli, F.T. Wagner, Appl. Catal. B Environ. 56 (2005) 9–35.
- [14] G. Du, X. Liu, Y. Zong, T.A. Hor, A. Yu, Z. Liu, Nanoscale 5 (2013) 4657–4661.
- [15] M. Hamdani, R. Singh, P. Chartier, Int. J. Electrochem. Sci. 5 (2010) 556–577.
- [16] A. Garsuch, A. Panchenko, C. Querner, A. Karpov, S. Huber, R. Oesten, Electrochem. Commun. 12 (2010) 1642–1645.
- [17] L. Mao, D. Zhang, T. Sotomura, K. Nakatsu, N. Koshiba, T. Ohsaka, Electrochim. Acta 48 (2003) 1015–1021.
- [18] M. Calegari, F. Lima, E. Ticianelli, J. Power Sources 158 (2006) 735–739.
- [19] T. Wang, C.-L. Chiang, P.-C. Li, Y.-K. Hsieh, C.-F. Wang, Chem. Eng. J. 244 (2014) 243–251.
- [20] C.S. Johnson, D.W. Dees, M.F. Mansuetto, M.M. Thackeray, D.R. Vissers, D. Argyriou, C.K. Loong, L. Christensen, J. Power Sources 68 (1997) 570–577.
- [21] C.-C. Yang, S.-T. Hsu, W.-C. Chien, M. Chang Shih, S.-J. Chiu, K.-T. Lee, C. Li Wang, Int. J. Hydrogen Energy 31 (2006) 2076–2087.
- [22] F. Cheng, T. Zhang, Y. Zhang, J. Du, X. Han, J. Chen, Angew. Chem. Int. Ed. 52 (2013) 2474–2477.
- [23] Y. Jeong, A. Manthiram, J. Electrochem. Soc. 149 (2002) A1419–A1422.
- [24] R.K. Sharma, H.-S. Oh, Y.-G. Shul, H. Kim, Phys. B Condens. Matter 403 (2008) 1763–1769.
- [25] J. Read, J. Electrochem. Soc. 149 (2002) A1190–A1195.
- [26] A.K. Thapa, T. Ishihara, J. Power Sources 196 (2011) 7016–7020.
- [27] E. Yeager, J. Mol. Catal. 38 (1986) 5–25.
- [28] F. Cheng, Y. Su, J. Liang, Z. Tao, J. Chen, Chem. Mater. 22 (2009) 898–905.
- [29] Y. Cao, H. Yang, X. Ai, L. Xiao, J. Electroanal. Chem. 557 (2003) 127–134.
- [30] M.M. Thackeray, Prog. Solid State Chem. 25 (1997) 1–71.
- [31] J. Xiao, D. Wang, W. Xu, D. Wang, R.E. Williford, J. Liu, J.-G. Zhang, J. Electrochem. Soc. 157 (2010) A487–A492.
- [32] M.O. Danilov, A.V. Melezhyk, J. Power Sources 163 (2006) 376–381.
- [33] X. Wang, Y. Li, J. Am. Chem. Soc. 124 (2002) 2880–2881.
- [34] R.B. Valim, M.C. Santos, M.R.V. Lanza, S.A.S. Machado, F.H.B. Lima, M.L. Calegari, Electrochim. Acta 85 (2012) 423–431.
- [35] M. Toupin, T. Brousse, D. Bélanger, Chem. Mater. 14 (2002) 3946–3952.
- [36] M.-Y. Cho, S.-M. Park, B.H. Choi, J.-W. Lee, K.C. Roh, J. Ceram. Process. Res. 13 (2012) s166–s169.
- [37] S. Devaraj, N. Munichandraiah, J. Solid State Electrochem. 12 (2008) 207–211.
- [38] E.P. Barrett, L.G. Joyner, P.P. Halenda, J. Am. Chem. Soc. 73 (1951) 373–380.
- [39] C.-C. Hu, C.-Y. Hung, K.-H. Chang, Y.-L. Yang, J. Power Sources 196 (2011) 847–850.
- [40] L. Wang, D.-L. Wang, Electrochim. Acta 56 (2011) 5010–5015.
- [41] J. Goldstein, A. Tseung, Nature 222 (1969) 869–870.
- [42] C.-L. Lee, Y.-L. Tsai, C.-H. Huang, K.-L. Huang, Electrochem. Commun. 29 (2013) 37–40.
- [43] R.R. Adžić, S. Strbac, N. Anastasijević, Mater. Chem. Phys. 22 (1989) 349–375.
- [44] W. Bian, Z. Yang, P. Strasser, R. Yang, J. Power Sources 250 (2014) 196–203.
- [45] I. Roche, E. Chaînet, M. Chatenet, J. Vondrák, J. Phys. Chem. C 111 (2006) 1434–1443.
- [46] Z.-S. Wu, S. Yang, Y. Sun, K. Parvez, X. Feng, K. Müllen, J. Am. Chem. Soc. 134 (2012) 9082–9085.
- [47] Y. Liang, Y. Li, H. Wang, J. Zhou, J. Wang, T. Regier, H. Dai, Nat. Materials 10 (2011) 780–786.
- [48] P.H. Matter, L. Zhang, U.S. Ozkan, J. Catal. 239 (2006) 83–96.
- [49] Z. Chen, A. Yu, R. Ahmed, H. Wang, H. Li, Z. Chen, Electrochim. Acta 69 (2012) 295–300.
- [50] G. Wu, P. Zelenay, Acc. Chem. Res. 46 (2013) 1878–1889.
- [51] T.C. Nagaiah, S. Kundu, M. Bron, M. Muhler, W. Schuhmann, Electrochem. Commun. 12 (2010) 338–341.
- [52] L. Mao, T. Sotomura, K. Nakatsu, N. Koshiba, D. Zhang, T. Ohsaka, J. Electrochem. Soc. 149 (2002) A504–A507.
- [53] B.D. McCloskey, R. Scheffler, A. Speidel, D.S. Bethune, R.M. Shelby, A. Luntz, J. Am. Chem. Soc. 133 (2011) 18038–18041.
- [54] M.S. El-Deab, T. Ohsaka, J. Electrochem. Soc. 153 (2006) A1365–A1371.
- [55] K. Gong, P. Yu, L. Su, S. Xiong, L. Mao, J. Phys. Chem. C 111 (2007) 1882–1887.

- [56] F. Garzon, I. Raistrick, E. Brosa, R. Houlton, B.W. Chung, *Sens. Actuators B Chem.* 50 (1998) 125–130.
- [57] H. Dietz, *Solid State Ionics* 6 (1982) 175–183.
- [58] R. Imran Jafri, N. Sujatha, N. Rajalakshmi, S. Ramaprabhu, *Int. J. Hydrogen Energy* 34 (2009) 6371–6376.
- [59] J.-J. Han, N. Li, T.-Y. Zhang, *J. Power Sources* 193 (2009) 885–889.
- [60] M. Lu, S. Kharkwal, H.Y. Ng, S.F.Y. Li, *Biosens. Bioelectron.* 26 (2011) 4728–4732.
- [61] P. Hernández-Fernández, S. Rojas, P. Ocón, A. de Frutos, J.M. Figueroa, P. Terreros, M.A. Peña, J.L.G. Fierro, *J. Power Sources* 177 (2008) 9–16.
- [62] T.-H. Yang, S. Venkatesan, C.-H. Lien, J.-L. Chang, J.-M. Zen, *Electrochim. Acta* 56 (2011) 6205–6210.
- [63] Y. Li, M. Gong, Y. Liang, J. Feng, J.-E. Kim, H. Wang, G. Hong, B. Zhang, H. Dai, *Nat. Commun.* 4 (2013) 1805.